Monthly Notices of the ROYAL ASTRONOMICAL SOCIETY

MNRAS **542,** 2167–2183 (2025)
Advance Access publication 2025 August 19

https://doi.org/10.1093/mnras/staf1376

MeerKAT-derived H I kinematics and the baryonic Tully–Fisher relation in the X-ray luminous cluster Abell 3408

Xola Ndaliso[1]★ Tariq Blecher[2,3] Roger P. Deane[1,4] and Ed Elson[5]

[1] *Wits Centre for Astrophysics, School of Physics, University of the Witwatersrand, 1 Jan Smuts Avenue, Johannesburg 2050, South Africa*
[2] *Centre for Radio Astronomy Techniques and Technologies, Department of Physics and Electronics, Rhodes University, PO Box 94, Makhanda 6140, South Africa*
[3] *South African Radio Astronomy Observatory, 2 Fir Street, Black River Park, Observatory, Cape Town 7925, South Africa*
[4] *Department of Physics, University of Pretoria, Hatfield, Pretoria 0028, South Africa*
[5] *Department of Physics and Astronomy, University of the Western Cape, Robert Sobukwe Rd, Bellville, Cape Town 7535, South Africa*

Accepted 2025 August 17. Received 2025 July 18; in original form 2024 November 12

ABSTRACT

Significant advances in observational capabilities are continuously transforming our understanding of the dense environment of galaxy clusters and its impact on individual galaxies. Discerning between the intrinsic and the externally induced properties of galaxies, including their gas kinematics, is a key diagnostic in the field of galaxy evolution. In this paper, we present MeerKAT H I spectral line observations of the redshift $z \sim 0.042$ galaxy cluster Abell 3408. A total of 64 galaxies are detected in H I in this X-ray luminous galaxy cluster ($L_X \sim 3 \times 10^{43}$ erg s^{-1}). We model the H I morphology and gas kinematics of the individual galaxies, using a semi-automated pipeline based on CANNUBI and pyBBarolo. The pipeline was developed and tested as part of this study. Of the 64 galaxies detected in the cluster, we successfully modelled 16, while the remaining galaxies exhibit disturbed H I morphologies, insufficient angular or velocity resolution. We combine the galaxies with converged kinematic fits with 67 field galaxies from the MeerKAT spectral line survey early science data ($\langle z \rangle = 0.0435$) to produce a measurement of the baryonic Tully–Fisher relation (bTFr) that encompasses a broader range of environment and provides a useful comparison. We find a slope ($\alpha = 3.66^{+0.32}_{-0.28}$) for this relation, which is consistent with that found from the MeerKAT International GHz Tiered Extragalactic Exploration (MIGHTEE) survey bTFr derived from the same definition. Interestingly, H I detections of the Abell 3408 galaxy cluster galaxies are seen to extend the bTFr of the MIGHTEE sample, both in mass and velocity, despite their cluster environment.

Key words: galaxies: clusters: general – galaxies: kinematics and dynamics.

1 INTRODUCTION

In the hierarchical structure-formation model, the construction of significant structures such as galaxy clusters occurs through the continuous process of merging and accretion of galactic haloes (see, e.g. Mantz et al. 2010; White, Cohn & Smit 2010; Wu, Rozo & Wechsler 2010; Tinker et al. 2011; Kravtsov & Borgani 2012; Wei 2016; Planck Collaboration et al. 2016; Caminha et al. 2022). Galaxies fall into clusters in radial orbits (see, e.g. Biviano et al. 2013; Munari, Biviano & Mamon 2014; Mamon et al. 2019) and become susceptible to diverse astrophysical processes imposed by the hot, ionized intracluster medium (ICM) of the dense environment. These astrophysical mechanisms have an impact on the equilibrium, morphologies, gas content and star-formation activity of the galaxies as they traverse the ICM (Serra et al. 2017).

The gas content of cluster galaxies is primarily influenced by environmental processes, including hydrodynamical mechanisms such as ram-pressure stripping, where cold gas is removed from the interstellar medium (ISM) by the hot ICM (e.g. Gunn & Gott 1972; Piraino-Cerda et al. 2023; O'Beirne et al. 2024; Vulcani et al. 2024) and by starvation (or strangulation), a process in which gas accretion on to the galaxy is halted after infall into a cluster halo, gradually quenching star formation over long time-scales (e.g. Cortese, Catinella & Smith 2021; Boselli, Fossati & Sun 2022). The former mechanism halts the star-formation activity in the galaxy disc on longer time-scales (∼4 Gyr; Boselli et al. 2014), compared to the latter, which ceases star formation on relatively short time-scales (∼100–200 Myr; Vollmer et al. 2004). However, recent studies suggest that, in some cases, ram-pressure-induced quenching may take place over longer time-scales of 1.5–3.5 Gyr, comparable to starvation (Marasco et al. 2023). Ram-pressure stripping, amongst other processes, has been reported to be the principal mechanism that reduces the star-formation rates in cluster galaxies (e.g. Koopmann & Kenney 2004). The loss of gas in cluster galaxies has been explained further with other processes that occur in galaxy clusters such as turbulent viscous stripping (e.g. Chung et al. 2007) and thermal evaporation (e.g. Nipoti 2010). The cold gas affected by these mechanisms includes neutral atomic hydrogen (H I) and the molecular gas, which can also experience environmental effects (e.g. Lee et al. 2016;

★ E-mail: xola.ndaliso@gmail.com

Brown et al. 2021; Boselli et al. 2022; Zabel et al. 2022). However, molecular gas and dust are generally more resilient compared with diffuse phases such as H I and ionized gas (e.g. Hα-emitting gas; Poggianti et al. 2017).

Over the past 60 yr, studies of galaxy rotation curves have played a pivotal role in our understanding of the matter distribution in galaxies, revealing a discrepancy between the observed velocities of stars and gas and those expected based solely on the visible matter, thereby providing the cornerstone of evidence for dark matter (e.g. Rubin, Ford & Thonnard 1978; Bosma 1981; van Albada et al. 1985). The distribution of dark matter in galaxies has been an open and long-standing question for several decades – the 'cusp/core' problem, as it is commonly called (de Blok et al. 2008).

Galaxy rotation curves have been put in the spotlight, in attempts to solve this discrepancy. Neutral hydrogen (H I) often extends to several optical diameters, tracing galaxy dynamics at large radii and into regions where dark matter is thought to dominate the dynamics of galaxies (de Blok & Bosma 2002; Blok et al. 2008; Swaters et al. 2012; Lelli, McGaugh & Schombert 2016; Mancera Piña et al. 2021; Laudage et al. 2024). H I follows nearly circular orbits in galaxies and, because of its diffuse and extended nature, serves as one of the leading tracers for studying the rotation curves of galaxies. However, historically, H I rotation curves have been limited to small samples of galaxies. It is only over the past two decades that we have seen an increase in high-resolution H I surveys of galaxies, such as The H I Nearby Galaxy Survey (THINGS; Walter et al. 2008), the Very Large Array survey of Advanced Camera for Surveys Nearby Galaxy Survey Treasury galaxies (VLA-ANGST; Ott et al. 2012), Local Irregulars That Trace Luminosity Extremes THINGS (LITTLE THINGS; Hunter et al. 2012) and the Local Volume H I Survey (LVHIS; Koribalski et al. 2018), enabling high-resolution rotation curves of local ($\lesssim$12 Mpc) galaxies. These surveys have enhanced the resolution of H I rotation curves, enabling the construction of high-quality mass models. For instance, Mancera Piña et al. (2022) developed resolved kinematic and mass models for 32 LITTLE THINGS galaxies, which form a subsample of the study conducted by Iorio et al. (2017) and a subset of nearby spiral galaxies analysed by Di Teodoro & Peek (2021).

Larger samples of high-quality, highly resolved H I rotation curves have, in turn, significantly advanced the study of the dynamical scaling relations such as the Tully–Fisher relation (TFr; Tully & Fisher 1977). The TFr is a dynamical relation that links a spiral galaxy's mass–luminosity to its rotation velocity. This relation has proven to be important in understanding galaxy formation and evolution, and several authors (e.g. Verheijen 2001; Lelli et al. 2016; Ponomareva et al. 2017) have studied the TFr across a broad class of galaxies. Chung et al. (2002) studied the TFr and showed that it holds for rotating galaxies of different morphologies. Similarly, Abril-Melgarejo et al. (2021), using optical observations, showed that the TFr holds for galaxies in dense environments at $z \sim 0.7$. Courteau et al. (2003) also studied the TFr for un/barred spiral galaxies, finding no correlation between the presence of a bar in a galaxy and its projection on the TF plane. This provided further insights that un/barred spirals have, on average, comparable fractions of luminous- and dark-matter fractions at a given radius.

At $z \sim 0$, Lelli et al. (2019) studied the baryonic TFr (bTFr; McGaugh et al. 2000) for 153 galaxies in the Spitzer Photometry and Accurate Rotation Curves (SPARC) data base, which consists of 175 spiral galaxies with high-quality H I rotation curves (Lelli et al. 2016). This is considered to be the largest observational study of the bTFr to date. In their work, Lelli et al. studied the bTFr based on different velocity definitions such as W_{50}, which is the rotational velocity measure derived from the integrated H I line profile, $V_{\rm flat}$, which is the velocity measured on the flat part of the H I rotation curve, and $V_{\rm max}$, which is the maximum measured rotational velocity from the H I rotation curve. The tightest bTFr with the steepest slope was achieved using the $V_{\rm flat}$ velocity definition. These results are in good agreement with recent studies of the bTFr based on SIMBA (see Davé et al. 2019) cosmological hydrodynamical simulations (Glowacki, Elson & Davé 2020). Ponomareva et al. (2021) used the Early Science data release of the MeerKAT International GHz Tiered Extragalactic Exploration (MIGHTEE) survey – see Jarvis et al. (2017) for details of the survey – to perform, for the first time, a homogeneous study of the H I-based bTFr over the last billion years ($0 \lesssim z \leq 0.081$) using a sample of 67 field galaxies. They considered two velocity measures: W_{50} from the corrected width of the H I global profile and $V_{\rm out}$, which is the rotational velocity measured at the outermost point of the resolved H I rotation curves. For both velocity definitions, they found relations with very low intrinsic scatter orthogonal to the best-fitting relation, comparable to the SPARC sample at $z \sim 0$. They also found that the slopes of the relations are consistent with several studies carried at $z \sim 0$.

Table 1. Summary of *L*-band MeerKAT observations of Abell 3408.

Observing dates	2019/05/11–2019/05/12
Pointing centre (J2000)	$07^{\rm h}08^{\rm m}31\overset{\rm s}{.}7$–$49^{\rm d}12^{\rm m}52^{\rm s}$
Number of antennas	61
On-source time	11.6 (h)
$t_{\rm int}$	8 (s)
Frequency range	856–1712 (MHz)
$\Delta\nu$	209 (kHz)
	46 km s^{-1} for H I at $z = 0.04$
H I cube weighting	`Briggs robust` 0.5
$\sigma_{\rm rms}$ per 209-kHz channel	85 (μJy beam^{-1})
$\theta_{\rm synth}$, BPA	13.1 × 11.7 arcsec^2, $-42\overset{\circ}{.}6$

In our work, we use MeerKAT H I spectral line observations of the redshift $z \sim 0.042$ galaxy cluster Abell 3408. For the first time, we model the kinematics of detected Abell 3408 cluster galaxies in a uniform way using a pipeline, developed as part of this work, based on CANNUBI and pyBBarolo. We successfully model the kinematics of 16 galaxies within this cluster. Furthermore, we use the converged kinematics models to study the H I-based bTFr, extending our sample with 67 MeerKAT MIGHTEE field galaxies from Ponomareva et al. (2021).

The structure of the paper is as follows. In Section 2 we describe the MeerKAT observations and data reduction, and present the H I data products of the Abell 3408 galaxy cluster. In Section 3 we discuss the H I kinematic modelling pipeline developed as part of this work, and we also present the rotation curves overlaid on position–velocity slices of the 16 modelled galaxies. The H I-based bTFr and the fitting procedure are discussed in Section 5, with summary and conclusions in Section 6. Throughout this work, we assume cosmological values $\Omega_{\rm M} = 0.311$, $\Omega_{\Lambda} = 0.688$, and $H_0 = 67.66$ km s^{-1} (Planck Collaboration VI 2018).

2 MEERKAT OBSERVATIONS AND DATA PROCESSING

Abell 3408 was observed with MeerKAT (Jonas et al. 2016) on 2019 May 11 and 12 with 61 antennas. The data were taken using the *L*-band receivers (900–1670 MHz), with a bandwidth of 856 MHz divided into 4096 channels (see Table 1). The 209-kHz channel width has an equivalent velocity width of ∼46 km s^{-1} at $z \sim 0.042$. The full observation duration was $\sim$11.6 h with integration time set to 8 s. J0408$-$6545 was used as a primary flux and bandpass calibrator, and was observed for 10 min after every 2-h scan of the target. The gain calibrator, J0825$-$5010, was observed for 2 min after every 1-min scan of the target.

2.1 Calibration and imaging

We process a bandwidth subset of 100 MHz, from 1300–1400 MHz, which encompasses all the individual cluster members as well as the candidate lensed H I source. The radio frequency interference (RFI) was flagged using the AOFLAGGER (Offringa 2010). We used an early version of the OXKAT data processing software for calibration (see Heywood et al. 2020 for full details). The antenna-based terms were solved for, in the following order: geometric delays, initial antenna gain phase, complex bandpass response, complex antenna gains (with the initial antenna gain phase discarded), and absolute flux scaling.

In the self-calibration step, we adopted an iterative approach between imaging, setting the `Briggs robust` parameter to -0.3, and phase-only self-calibration using a solution interval of 20 s. Overall flagging percentages of $\sim$10 per cent in both XX and YY polarizations, across the 100-MHz bandwidth, were measured after calibration. This percentage is significantly lower than the typical full band amounts; this is because 100 MHz is in a generally clean region within the *L* band.

The continuum emission across the 100-MHz bandwidth was imaged and modelled using WSCLEAN (Offringa 2010) to create a multifrequency synthesis (MFS) image with four 25-MHz sub-bands. A multistage approach was adopted for the deconvolution step. Initially, an MFS continuum image was created using auto-masking with the masking threshold set to $10\sigma_{\rm global}$, where $\sigma_{\rm global}$ is the global rms of the entire image. Secondly, using the DDFACET package (Tasse et al. 2018), a static mask was derived from this image. To avoid artefacts with bright sources, a local rms threshold of $6\sigma_{\rm local}$ was used (Heywood et al. 2020). Thirdly, a new MFS continuum image was created using the static mask as well as the auto-masking with a similar setting as before. Lastly, the image was manually inspected, and we found that the procedure successfully deconvolved both low- and high-brightness sources.

To remove the continuum emission, we subtracted a frequency-linear continuum visibility model from the calibrated visibilities. A CLEAN cube is then generated with WSCLEAN using an auto-masking threshold of $5\sigma_{\rm global}$. To mitigate the residual continuum in the emission cube, we then performed image-plane continuum subtraction by fitting a frequency-dependent first-order polynomial to each pixel with the CASA task IMCONTSUB. After this step, the continuum artefacts were largely within the thermal noise level. With the resulting cube, we reached a 209-kHz channel noise of 85 μJy beam^{-1} using `Briggs robust` of 0.5 weighting.

To correct the effect of the primary beam, we generated a MeerKAT primary beam model with the EIDOS package (Asad et al. 2021). The parameters were set to produce a Stokes I beam model with the same frequency and angular dimensions as the data cube. The data cube was then corrected by dividing the intensity of each pixel, with the size of 3 arcsec, by the Stokes I beam model at that position. The resulting PSF FWHM is 13.1×11.7 arcsec^2 and the position angle (PA) is $-42\overset{\circ}{.}6$ east of north.

2.2 Source finding and cross-matching

The Source Finding Application (SOFIA; Serra et al. 2015) was run on the final primary-corrected beam cube, to extract the spectral line detections and source properties. SOFIA offers several functions to improve the reliability of detections. The procedure used in this work is as follows:

(i) smoothing the cube iteratively and extracting only pixels above a certain threshold;
(ii) merging the pixels to a detection threshold;
(iii) reliability filtering;
(iv) mask dilation;
(v) source parametrization.

The cube was smoothed using a boxcar convolution with angular and frequency sizes up to (30 arcsec, 209 kHz). To ensure that not only bright pixels were extracted and to enable reliability calculation, the detection threshold was set to 3.8σ following iterative manual testing. Pixels with flux greater than this threshold were merged to the same source if separated by less than 18 arcsec and 90 km s^{-1}. False positives were filtered out by using the built-in reliability filter, with a reliability threshold of 90 per cent and a signal-to-noise ratio (S/N) cut of 15 (see Serra et al. 2015 for more details).

Following this procedure, a total of 64 H I detections, presented in Fig. 1, were found in the Abell 3408 galaxy cluster. We then cross-matched the H I detections with the four mid-infrared bands (3.4, 4.6, 12, and 22 μm) of the *Wide-field Infrared Survey Explorer* (*WISE*) All-Sky Survey (Wright et al. 2010). As the H I distribution can be off-centre from its host galaxy due to environmental factors, we cross-matched the catalogue manually by overlaying the H I intensity maps on the W1 and DSS *R*-band maps (Fig. 2).

Of the 64 MeerKAT H I detections in Abell 3408, we find counterparts for 55 sources ($\sim$86 per cent) in the 3.4 μm (W1) band, 50 sources ($\sim$78 per cent) in the 4.6 μm (W2) band, 41 sources ($\sim$64 per cent) in the 12 μm (W3) band, and 25 sources ($\sim$39 per cent) in the 22 μm (W4) band.

3 H I PROPERTIES OF THE MEERKAT DETECTIONS

The MeerKAT H I zeroth-order moment map of the Abell 3408 galaxy cluster showing all 64 detections is presented in Fig. 1. This moment map is generated by SOFIA across the masked H I data cube.

We observe that the majority of sources are positioned in the north-western region of the galaxy cluster. This distribution may be influenced by the neighbouring galaxy cluster, Abell 3407, which was reported to interact with Abell 3408 (Nascimento et al. 2016). The MeerKAT observations increase the number of known cluster members in the Abell 3408 galaxy cluster from the 27 galaxies previously reported in Nascimento et al. (2016).

We present MeerKAT H I moment-zero maps of four detections that are representative of the H I morphologies in the cluster in physical units of H I surface densities (i.e. M$_\odot$ pc^{-2}). To convert the map from the flux units of Jy beam^{-1} Hz to units of Jy km s^{-1} we divide the moment-zero map by the channel width ($\Delta\nu$) in Hz, given in Table 1, and multiply by the channel width in km s^{-1}, which results in a moment-zero map in units of Jy beam^{-1} km s^{-1}. To obtain the map in Jy km s^{-1} we then divide by the beam area over the pixel area (see equation 3 of Iorio et al. 2017). This results in a map of units of Jy km s^{-1}, which can be converted to units of M$_\odot$ using equation (1). This is then divided by the physical area of the pixel in pc^2, resulting in a moment-zero map with units of M$_\odot$ pc^{-2}. Of these four detections shown in Fig. 3, the first detection (i.e. top left) is identified with ID 9 in the MeerKAT H I cluster moment-zero map shown in Fig. 1, found with three other potential companions in close proximity, with a stellar mass of $\log_{10}(M_*) = 11.13$ M$_\odot$. The

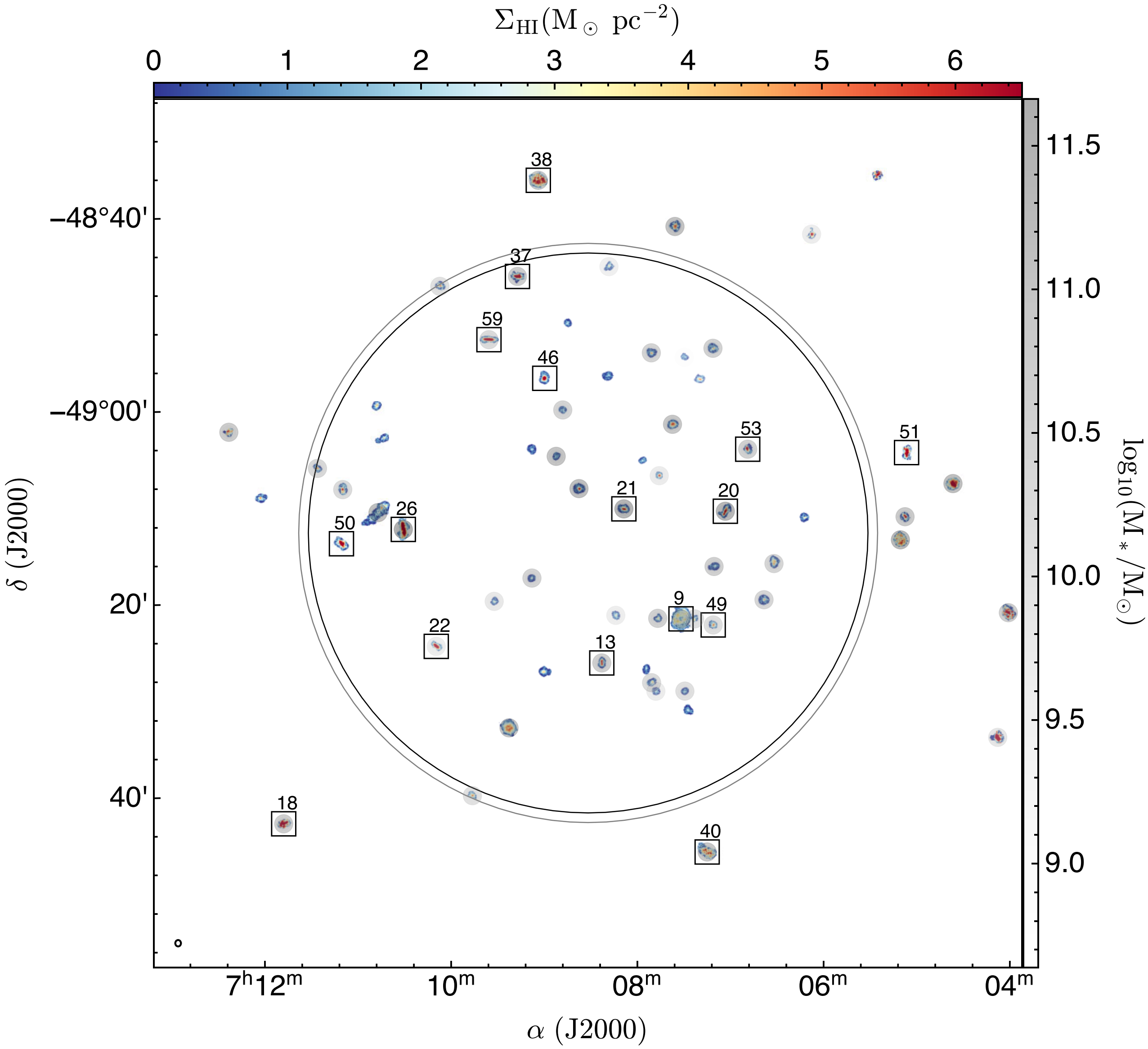

Figure 1. The MeerKAT H I moment-zero map of the Abell 3408 galaxy cluster showing all 64 detections coloured by the H I mass surface density. Galaxies with W1 (3.4 μm) and W2 (4.2 μm) counterparts are shown with the grey shaded circles, coloured with M_* of each galaxy. The black squares mark the 16 galaxies with converged kinematic fits. The MeerKAT synthesized beam (13.1 × 11.7 arcsec^2) is shown in the bottom-left corner. The black circle presents the MeerKAT Stokes I primary beam half-maximum sensitivity and the grey circle marks the cluster radius (R_{200} = 1.5 Mpc).

MeerKAT H I moment-zero map of this source shows a significant drop in H I surface densities in the central part of the disc. For the H I moment maps, we follow the method outlined by Verheijen & Sancisi (2001) and Lelli, Verheijen & Fraternali (2014) to determine the outermost H I contour level. In line with the approach of Iorio et al. (2017), we construct an S/N map for each galaxy and compute the mean value of the pixels with S/N between 2.75 and 3.25. This mean is then adopted as the 3σ pseudo-level, denoted as $\sigma_{\rm 3T}$.

The second detection shown in Fig. 3, identifies with ID 21 in Fig. 1, which is seen almost at the cluster's centre, at a projected distance of $d_{\rm proj}$ = 0.24 Mpc, with no immediate neighbouring detections, and a stellar mass of $\log_{10}(M_*) = 11.48\,\rm M_\odot$. The majority of the H I mass is concentrated in the centre of this galaxy, with contours showing signs of marginal disturbance on the H I disc, which might be induced by the ICM. This is seen from the second contour at $3\,\rm M_\odot\,pc^{-2}$, which is asymmetric along the minor axis of this source. The third moment-zero map is an example of a galaxy undergoing ram-pressure stripping. This detection is ID 52 in Fig. 1, with a stellar mass of $\log_{10}(M_*) = 11.17\,\rm M_\odot$, and it seems to be undergoing or to have undergone ram-pressure stripping. The H I gas in this galaxy appears to be stripped by the ICM, forming a long H I tail. Additionally, at least based on the H I moment-zero map of this galaxy, gas accretion via merger could also be driving this extended H I tail. The last moment-zero map is that of detection ID 59, which is also seen to be isolated from Fig. 1. The inner H I disc of this source does not show any signs of disturbances (i.e. it is regular). However, well outside the stellar radius, the contours show that this galaxy might be experiencing some astrophysical mechanisms imposed by the ICM. The rest of the MeerKAT H I moment-zero maps for all the 64 galaxies are presented in Appendix A.

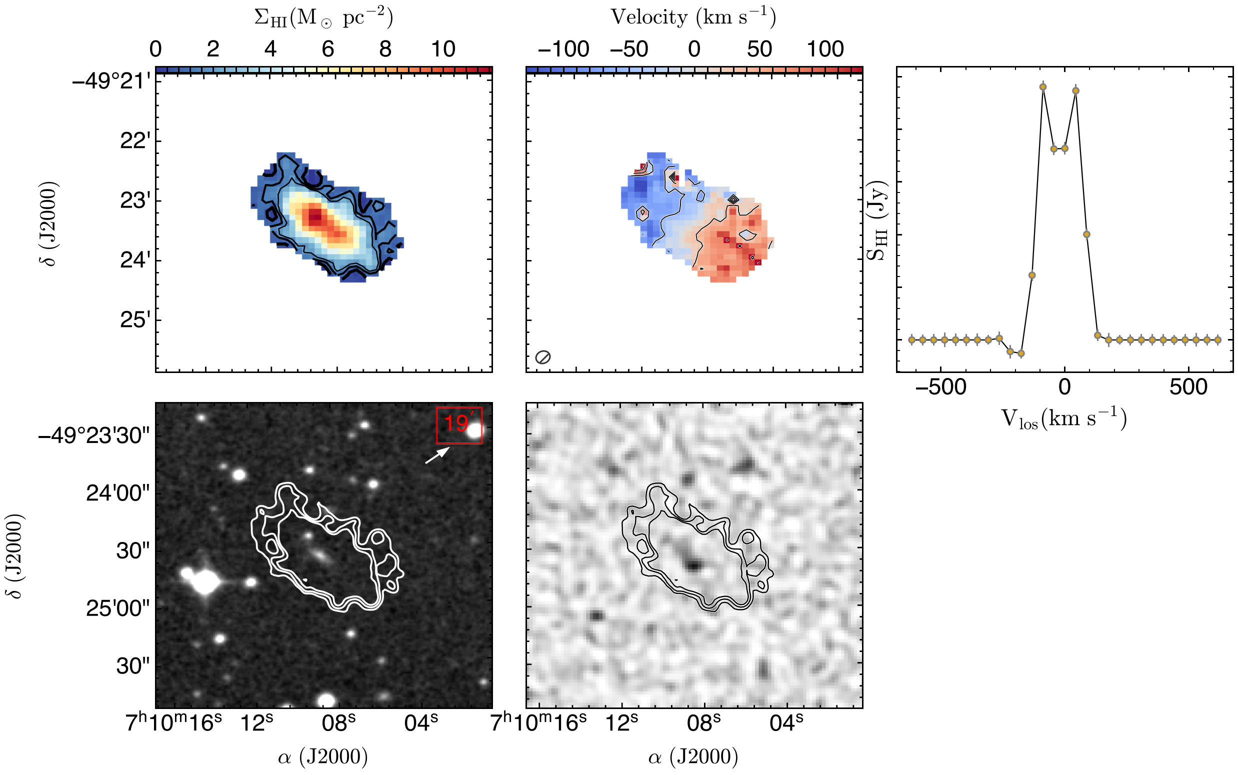

Figure 2. The top-left panel shows the MeerKAT H I intensity map of the galaxy where source ID 22 is presented with contour levels at 1, 2, and $3\sigma_{3\rm T}$ M$_\odot$ pc^{-2}. The top-middle panel shows the H I velocity field of the same galaxy. The top-right panel shows the integrated H I spectrum in the upper-right corner, with uncertainties calculated as the rms of each channel in the H I data cube. The bottom-left panel shows the DSS *R*-band image with H I contours overlaid. The distance in arcmin and the direction to the cluster centre are shown by the red text in the box and the white arrow, respectively. The bottom-middle panel shows the radio continuum image, in greyscale, of the same detected galaxy, overlaid with H I contours.

SOFIA also provides the zeroth-order and first-order moment maps for all the detected sources. These maps, similar to Fig. 1, are derived from the masked cube corresponding to each source. In Fig. 2 we present both the H I zeroth-order and first-order moment maps of one of the detected sources (SOFIA source ID 22) in the MeerKAT H I data cube. We also present the MeerKAT H I integrated spectrum for this source. For each of the 16 galaxies with converged kinematic models, we calculate the w_{50} (full width at 50 per cent peak flux) in km s^{-1} and these values are presented in Table 2.

3.1 Galaxy masses

Following Iorio et al. (2017) we calculate the H I mass for each of the H I detected sources using

$$\frac{M_{\rm H\,I}}{\rm M_\odot} = 23.5\left(\frac{\delta}{\rm arcsec}\right)^2\left(\frac{D}{\rm Mpc}\right)^2\sum_{\rm pixels}\left[\frac{\Sigma_{\rm obs}(x,y)}{\rm M_\odot\,pc^{-2}}\right], \qquad (1)$$

where δ is the size of the pixel, and D is the cosmological luminosity distance of the galaxy cluster. Over 50 per cent of the H I detections have $9.0 \le \log_{10}(M_{\rm H\,I}/{\rm M_\odot}) \le 10$, as shown in Fig. 4.

For the 48 H I detections with counterparts in both the W1 and W2 bands, we calculated the stellar masses (M_*) using equation (1) from Cluver et al. 2014,

$$\log_{10}\left(\frac{M_*}{L_{\rm W1}}\right) = -1.97(W_{3.4\,\mu\rm m} - W_{4.6\,\mu\rm m}) - 0.03,$$
$$\frac{L_{\rm W1}}{\rm L_\odot} = 10^{-0.4(M-M_\alpha)}, \qquad (2)$$

where M is the absolute magnitude of the source in W1 and $M_\alpha = 3.24$.

The calculated stellar masses of the 16 galaxies with converged kinematic models are presented in Table 2 and the distribution of M_* for all the galaxies with *WISE* counterparts is presented in Fig. 4. We adopt an indicative uncertainty of ∼0.1 dex for the calculated stellar masses (Ponomareva et al. 2021), which is consistent with the reported uncertainty of *WISE* stellar masses $\log_{10}(M_*/{\rm M_\odot}) > 10$ (see Jarrett et al. 2023). Additionally, the total dynamical masses presented in Table 2 are calculated using equation (10) from Yu, Ho & Wang (2020),

$$M_{\rm dyn} = \frac{V_{\rm rot}^2\,R_{\rm H\,I}}{G} = 2.33\times10^5\,{\rm M_\odot}\left[\frac{V_{\rm rot}^2\,R_{\rm H\,I}}{({\rm km\,s^{-1}})^2\,{\rm kpc}}\right], \qquad (3)$$

where G is the gravitational constant and $V_{\rm rot}$ is the H I rotation curve point, at radius $R_{\rm H\,I}$.

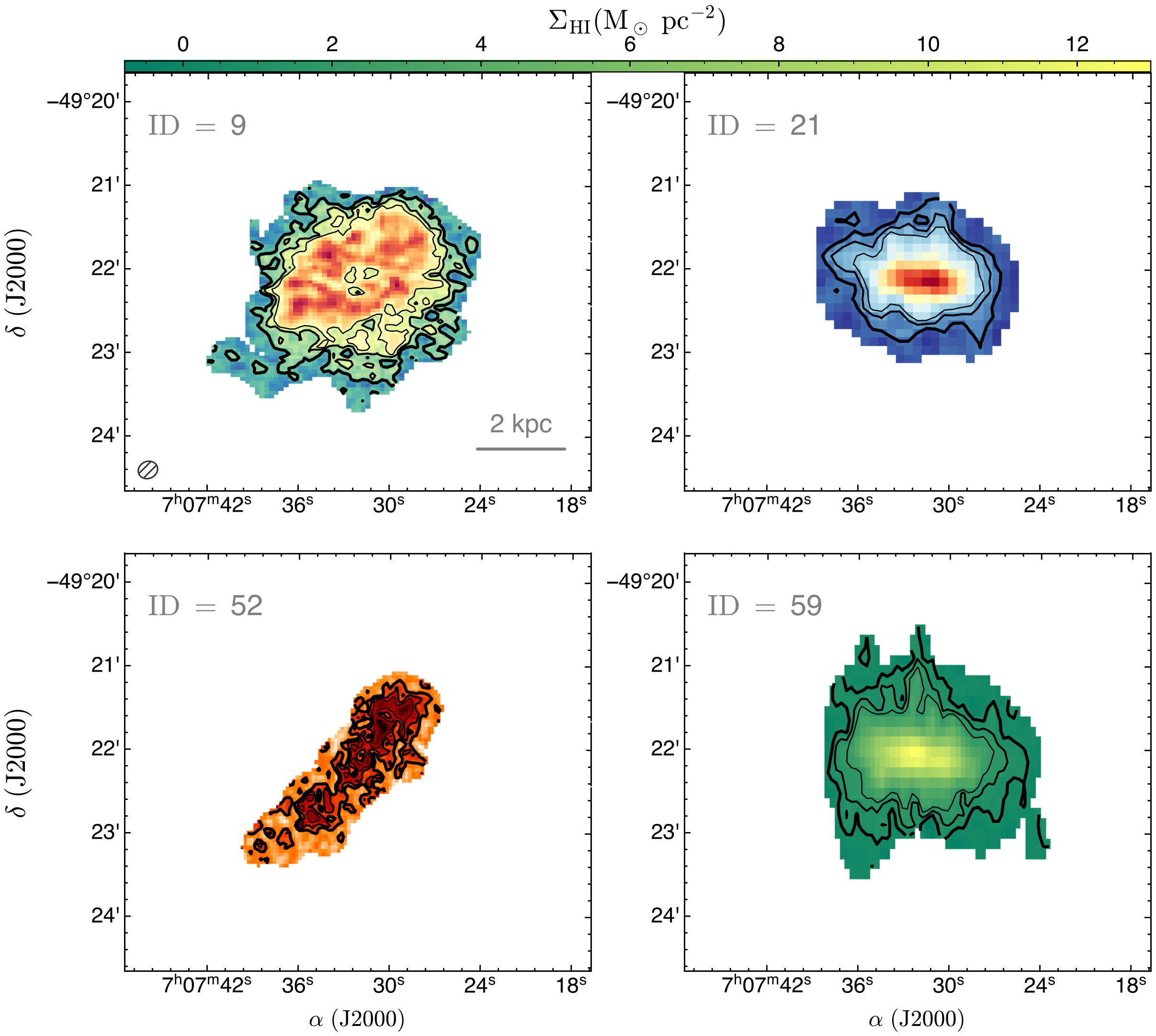

Figure 3. MeerKAT H I moment-zero maps of four sources that are representative of the 64 detected galaxies. The contour levels, with decreasing linewidth, trace H I surface densities at 1, 2, and $3\sigma_{3\rm T}$ M$_\odot$ pc^{-2}. The MeerKAT synthesized beam (13.1 × 11.7 arcsec^2) is displayed in the top-left panel, with the grey horizontal bar indicating the corresponding physical scale.

3.2 H I gas fractions

We use the H I and stellar masses to calculate the H I gas fractions of the individual galaxies, defined as

$$f_{\rm g} = \frac{M_{\rm H\,I}}{M_*}. \tag{4}$$

The calculated H I gas fractions are presented in Fig. 5, with respect to the projected distance ($d_{\rm proj}$) from the cluster centre. We notice a loose trend, such that galaxies in closer proximity (i.e. $d_{\rm proj} < 0.5$) to the centre of the cluster have lower gas fractions, and this is seen to increase with the projected distance. A similar result was also found in the studies of Zabel et al. (2022) and Moretti et al. (2023). We perform a linear fit of the following form,

$$f_{\rm g} = \alpha d_{\rm proj} + \beta, \tag{5}$$

where we achieve $\alpha = 0.04$, $\beta = 0.88$, and a scatter of 0.012. The fitted positive gradient suggests that these galaxies are progressively losing their H I content, likely due to some environmental effect.

In addition to this, we calculated the H I deficiency parameter of the galaxies with *WISE* counterparts. H I deficiency is the difference between the H I observed and expected mass in an isolated galaxy of the same size and morphology (Haynes, Giovanelli & Chincarini 1984). It serves as a quantity that indicates the amount of H I gas in a galaxy. We use equation (6) to calculate the expected H I mass, which correlates the observed M_* of a galaxy (see, e.g. Catinella et al. 2018; Parkash et al. 2018):

$$\log M_{\rm H\,I} = 0.51(\log M_* - 10) + 9.71. \tag{6}$$

For the H I detections with *WISE* counterparts, the H I deficiency ranges from −0.5 to ∼1.2, with more than 50 per cent of the Abell 3408 galaxies falling in the H I deficiency region (i.e. having $\text{def}_{\rm H\,I} > 0.3$; see Dénes, Kilborn & Koribalski 2014; Reynolds et al. 2020). About 39 per cent of the galaxies are found in the normal H I content regime (i.e. $-0.3 < \text{def}_{\rm H\,I} < 0.3$), and only 4 per cent of the galaxies have excess H I.

Table 2. Properties of the 16 galaxies with converged kinematic fits.

ID (1)	α (J2000) (h:m:s) (2)	δ (J2000) (d:m:s) (3)	$\log(M_{\mathrm{H\,I}})$ ($\mathrm{M_\odot}$) (4)	$\log(M_{\mathrm{dyn}})$ ($\mathrm{M_\odot}$) (5)	$\log(M_*)$ ($\mathrm{M_\odot}$) (6)	w_{50} (km s^{-1}) (7)	$z_{\mathrm{H\,I}}$ (8)	$d_{\mathrm{H\,I}}$ (kpc) (9)	$f^{*}_{\mathrm{H\,I}}$ (10)	$f^{\mathrm{dyn}}_{\mathrm{H\,I}}$ (11)
41	7 04 40.584	−49 07 0.583	10.2 ± 0.01	11.3 ± 0.06	11.2 ± 0.12	95.4 ± 20.5	0.043	72.1 ± 9.4	0.91 ± 0.02	0.91 ± 0.12
53	7 06 50.738	−49 04 0.544	9.6 ± 0.05	10.9 ± 0.05	10.6 ± 0.12	328.3 ± 34.8	0.043	36.2 ± 7.0	0.9 ± 0.11	0.88 ± 0.14
20	7 07 4.704	−49 10 4.903	9.8 ± 0.02	11.2 ± 0.05	11.4 ± 0.12	580.0 ± 59.0	0.044	51.7 ± 7.9	0.86 ± 0.04	0.88 ± 0.11
49	7 07 12.086	−49 22 2.018	9.5 ± 0.01	11.2 ± 0.05	10.2 ± 0.12	128.4 ± 19.8	0.043	36.2 ± 7.0	0.93 ± 0.02	0.85 ± 0.1
40	7 07 15.322	−49 45 3.355	10.2 ± 0.02	11.3 ± 0.05	11.0 ± 0.12	323.3 ± 34.3	0.047	82.2 ± 10.2	0.93 ± 0.04	0.9 ± 0.11
50	7 07 23.957	−49 21 4.881	10.1 ± 0.03	11.6 ± 0.05	–	292.9 ± 31.5	0.044	61.9 ± 8.6	–	0.87 ± 0.12
9	7 07 32.609	−49 21 4.913	10.4 ± 0.02	10.9 ± 0.05	11.1 ± 0.12	361.9 ± 37.9	0.045	112.6 ± 12.8	0.93 ± 0.04	0.95 ± 0.11
21	7 08 9.061	−49 10 2.029	9.7 ± 0.03	10.7 ± 0.05	11.5 ± 0.12	338.3 ± 35.7	0.044	41.4 ± 7.3	0.84 ± 0.05	0.91 ± 0.11
13	7 08 23.014	−49 26 9.881	9.6 ± 0.04	10.3 ± 0.07	10.7 ± 0.12	375.6 ± 39.2	0.045	41.4 ± 7.3	0.9 ± 0.07	0.93 ± 0.16
46	7 08 23.014	−49 26 9.881	9.9 ± 0.02	11.7 ± 0.06	–	188.2 ± 22.8	0.043	46.6 ± 7.6	–	0.84 ± 0.11
38	7 09 2.971	−48 36 9.699	10.4 ± 0.02	11.1 ± 0.05	10.9 ± 0.12	229.1 ± 26.0	0.044	92.4 ± 11.0	0.96 ± 0.04	0.94 ± 0.11
37	7 09 16.174	−48 46 7.1000	9.9 ± 0.02	11.2 ± 0.05	10.8 ± 0.12	338.0 ± 35.7	0.042	51.7 ± 7.9	0.92 ± 0.04	0.89 ± 0.11
59	7 09 34.243	−48 52 9.544	10.0 ± 0.01	11.3 ± 0.05	10.3 ± 0.12	292.5 ± 31.5	0.041	41.4 ± 7.3	0.98 ± 0.02	0.89 ± 0.10
22	7 10 8.491	−49 24 4.344	9.9 ± 0.03	10.5 ± 0.06	9.7 ± 0.12	203.7 ± 24.0	0.044	51.7 ± 7.9	1.02 ± 0.07	0.94 ± 0.14
26	7 10 29.009	−49 12 6.182	10.4 ± 0.02	10.6 ± 0.05	11.7 ± 0.12	422.9 ± 43.7	0.044	82.2 ± 10.2	0.89 ± 0.04	0.98 ± 0.12
18	7 11 46.922	−49 42 9.579	10.2 ± 0.01	11.4 ± 0.05	10.7 ± 0.12	276.4 ± 30.1	0.044	61.9 ± 8.6	0.95 ± 0.03	0.9 ± 0.10

Notes. Columns (2) and (3) show RA and Dec. (J2000) coordinates of the detections from SOFIA. Columns (4)–(6) show $\log(M_{\mathrm{H\,I}})$ calculated from the H I moment maps of the detections, $\log(M_{\mathrm{dyn}})$ estimated from the last measured point of the H I rotation curves, and $\log(M_*)$ estimated from *WISE*. Columns (7)–(9) show w_{50} from the SOFIA, H I redshifts, and H I diameters measured at $1\,\mathrm{M_\odot\,pc^{-2}}$. Columns (10) and (11) show H I to stellar, and dynamical mass fractions.

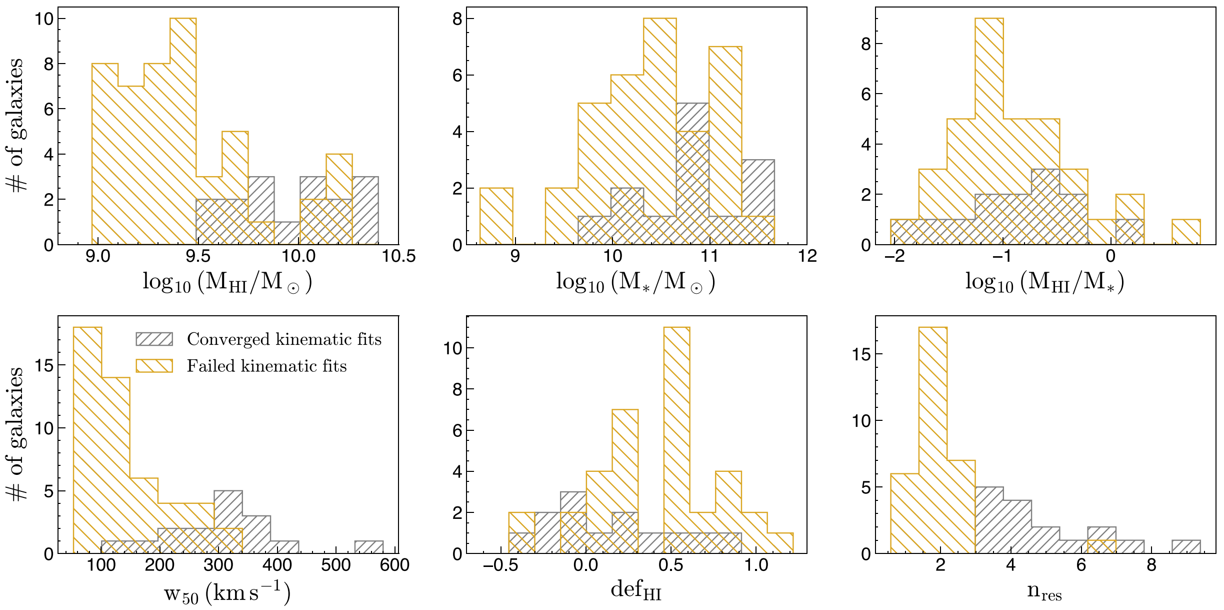

Figure 4. Properties of the MeerKAT H I detections in the Abell 3408 galaxy cluster. The 16 H I detections with converged kinematics fits are shown in grey, and the yellow shading presents the unmodelled detections.

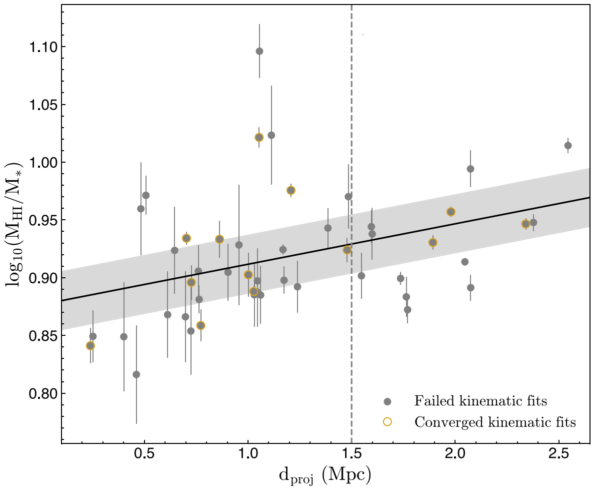

Figure 5. H I gas fraction of the detections with calculated stellar mass with respect to the galaxy's projected cluster-centric distance. The black line presents a linear fit, with 2σ scatter shown in grey. The points with yellow annuli mark the galaxies with converged kinematic fits.

4 H I KINEMATICS

We examine how the dense cluster environment may influence the H I kinematics of individual galaxies detected in Abell 3408. To model the H I kinematics of the individual galaxies in Abell 3408, we use the 3D tilted ring fitting software, ^{3D}BAROLO (di Teodoro & Fraternali 2015). This software fits a tilted-ring model (Rogstad, Lockhart & Wright 1974) on to the H I data cube. A principal feature of the software is that it creates a synthetic data cube based on the input observed cube. Following a ring-by-ring approach, the synthetic data cube is fitted to the H I data cube. The algorithm iterates through this step, minimizing residuals between the data and the model cube. Each of these rings is defined by a set of these kinematic and geometric parameters:

(i) the kinematic centre coordinates in pixels (x_0, y_0);
(ii) $V_{\rm rot}$, the gas rotation velocity along circular orbits;
(iii) $V_{\rm sys}$, the systemic velocity of the galaxy, due to the Hubble flow and its peculiar velocity;
(iv) ϕ, the disc PA, measured counterclockwise from the north to the major axis of the galaxy;
(v) i, the inclination angle of the gas disc, in the sky plane with respect to a face-on circular disc;
(vi) z_0, the scaleheight of the galaxy disc;
(vii) Σ, face-on H I column density;
(viii) $\sigma_{\rm H\,I}$, velocity dispersion.

The user can provide initial estimates for each of the parameters, although ^{3D}BAROLO can also make initial estimates automatically. These parameters can be left to change for each ring, or can be fixed.

4.1 Modelling approach

We develop a pipeline based on CANNUBI[1] (Roman-Oliveira, Fraternali & Rizzo 2023) and pyBBarolo[2] to model the H I kinematics of a large sample of marginally resolved galaxies. This standardized, automated approach is crucial for ensuring both reproducibility and scalability, especially given the growing number of spatially resolved galaxies observed with MeerKAT.

CANNUBI is a Python-based tool that uses the Markov chain Monte Carlo (MCMC) sampler EMCEE (Foreman-Mackey et al. 2013) to robustly determine the geometric parameters of galaxy discs. It estimates the coordinates of the centre (x_0, y_0), the radial extent, the thickness z_0, the PA and the inclination angle i of the galaxy's disc.

---

[1] https://www.filippofraternali.com/cannubi

[2] https://editeodoro.github.io/Bbarolo/pyBBarolo/

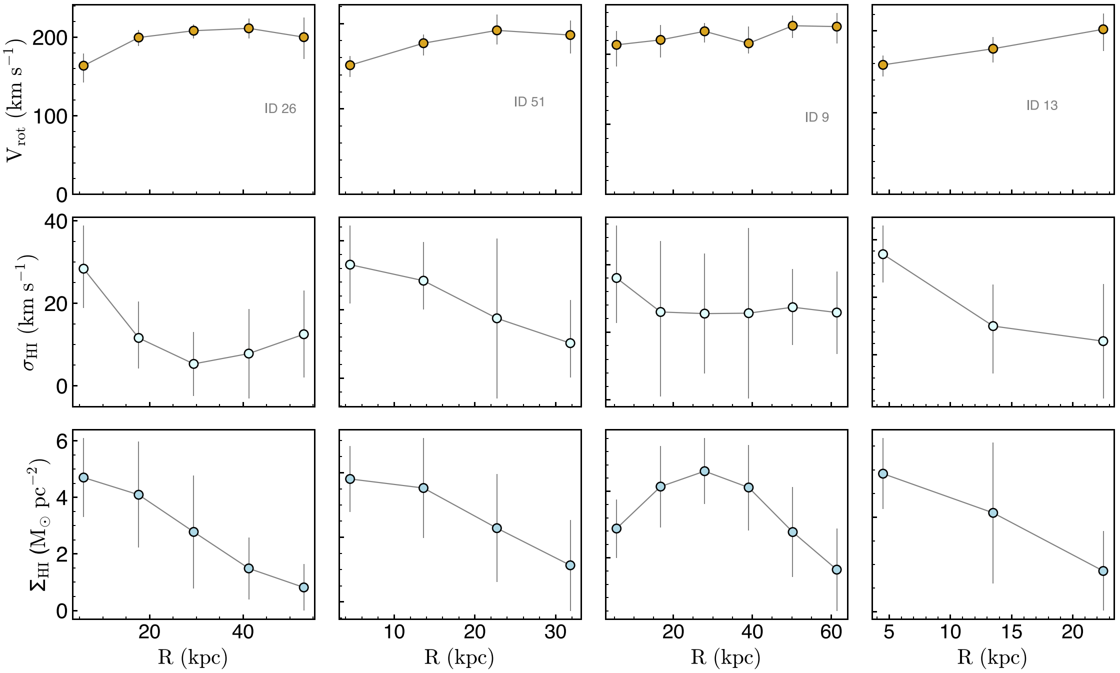

Figure 6. Data for four galaxies representative of the sample of modelled galaxies. The top row presents the H I rotation curves, the H I velocity dispersion profile is on the middle row, and the radial H I surface density profiles are shown in the bottom panel.

For more technical details, we refer the reader to Roman-Oliveira et al. (2023). pyBBarolo is a recently developed Python wrapper of the main $^{\rm 3D}$BAROLO class.

In the first stage of our pipeline, pyBBarolo is executed in blind mode, meaning that all initial parameter estimates are derived automatically from the input data cube. The kinematic centre coordinates are derived from the zeroth-order moment map (H I total intensity map) as the flux-weighted average positions of the source. The inclination angle of the H I disc is estimated by fitting a model map, to the observed zeroth-order moment (H I total intensity) map. The PA is estimated from the H I velocity field as the line that maximizes the velocity gradient along the line of sight. An initial estimate of the systemic velocity is derived as the central velocity from the global H I spectrum. The rotation velocity is also derived from the integrated H I spectrum, following

$$V_{\rm rot} = \frac{0.5 W_{20}}{\sin i}, \qquad (7)$$

where W_{20} in km s^{-1} is the width of the integrated H I spectrum at 20 per cent of the peak flux and i is the inclination angle of the H I disc.

For all the galaxies, we fixed $\sigma_{\rm H\,I} = 8$ km s^{-1}. We minimize $|mod - obs|$, where mod is the synthetic data cube and obs is the MeerKAT H I datacube, for each detected galaxy. The bulk of rotational information in a galaxy is contained in points closer to the major axis and thus for all our models we used the $\cos^2\theta$ weighting function where θ is the azimuth angle. We use `AZIM` for normalization of the 3D model and set `SNRCUT` and `GROWTHCUT` parameters to 3.5 and 3, respectively. The outputs of this first blind run are then used to generate parameter files, for each galaxy.

In the second step of the pipeline, the parameter files generated in the first step are used as input to run CANNUBI for each galaxy. The routine fits the central coordinates (x_0, y_0), inclination, PA, and ring separation (`RADSEP`) using 30 MCMC walkers over 1000 iterations. Key CANNUBI configuration parameters are set as follows: the masking method is set to `SMOOTH&SEARCH`, the noise level is computed dynamically for each data cube, the `FACTOR` is fixed at 1.5, `BLANKCUT` at 3, `SNRCUT` at 3.5, and `GROWTHCUT` at 2. The resulting fitted parameters are saved in an output file specific to each galaxy.

In the final step, we use the fitted parameters from CANNUBI to model the H I rotation curves of the galaxies with pyBBarolo. This step is configured similarly to the initial blind run, except that the inclination, PA, and ring width (`RADSEP`) are fixed to the values obtained from CANNUBI. We adopt an initial value of 8 km s^{-1} for the velocity dispersion ($V_{\rm disp}$), which is fitted simultaneously with the rotation curve (Fig. 6).

Among the 64 H I detections, only 19 galaxies span at least three independent resolution elements. We exclude galaxies with fitted inclination angles below 30°. After applying this criterion, 16 galaxies remain, for which we successfully construct H I kinematic models.

4.2 Results

Fig. 7 presents a comparison of the data with best-fitting kinematic models. As seen in Fig. 7, the best-fitting models reproduce reasonably well with the emission for each of the modelled galaxies. In Fig. 8, we present channel-by-channel comparison of the data and the $^{\rm 3D}$BAROLOkinematic model for a single galaxy. The model effectively reproduces the observed emission. Table 2 presents properties of the 16 galaxies with converged H I kinematic models. Two galaxies (IDs 40 and 46) were excluded from our sample of modelled galaxies for subsequent analysis. These galaxies exhibit kinematic models with unphysical rotation curves, based on visual inspection. Furthermore, the H I moment maps of both galaxies display disturbed morphologies, supporting their exclusion. The derived rotation curve data outer points for all the modelled galaxies are presented in Table 3.

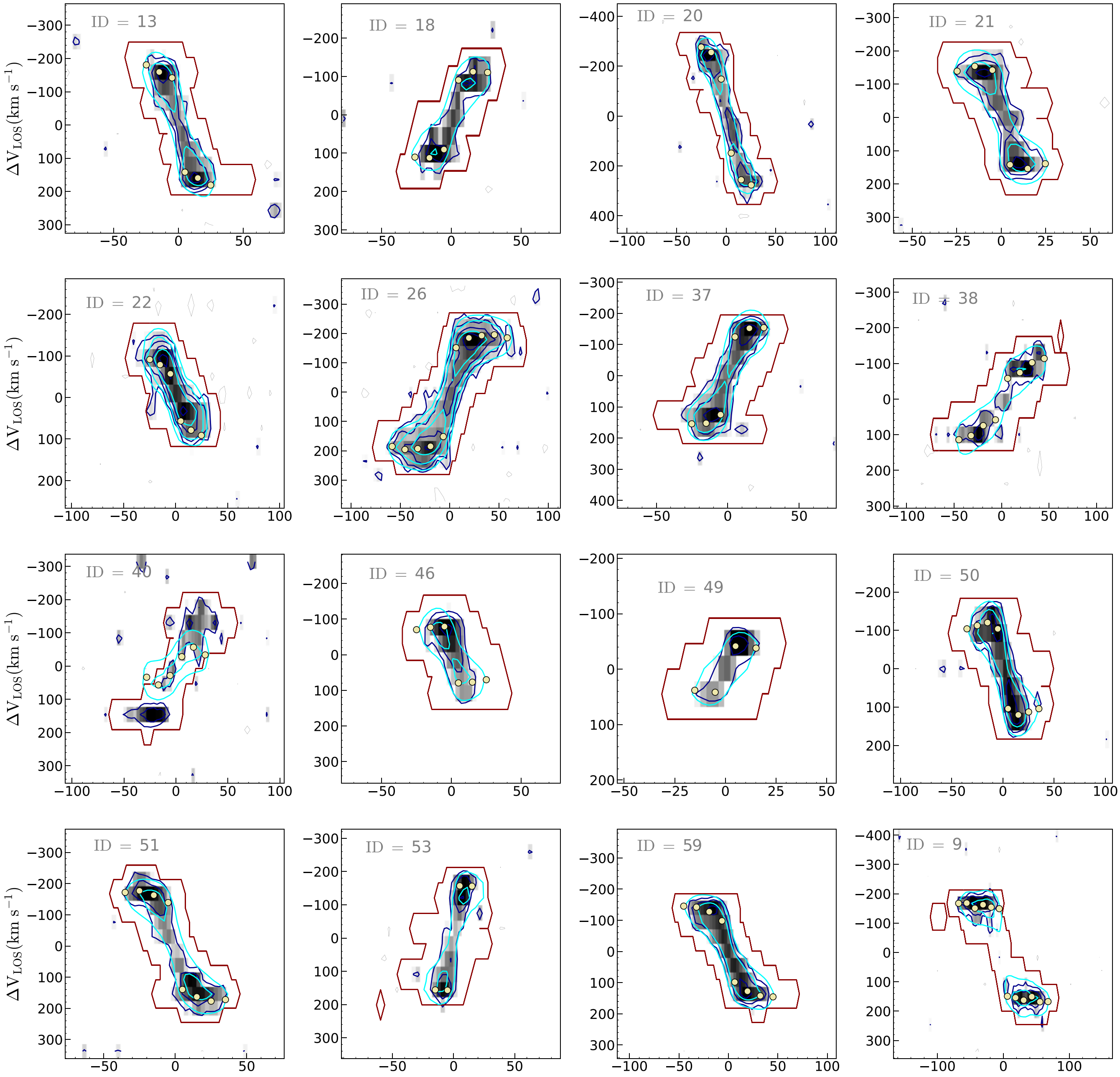

Figure 7. Rotation curves (yellow dots) of the 16 modelled galaxies overlaid on the H I major-axis position–velocity slices (greyscale with dark-blue contours). The cyan contours present the major-axis position–velocity slice extracted from the $^{\rm 3D}$BAROLO model, with the mask shown with maroon contours. The contour levels begin at $S_{\rm H\,I} = 188.4$ μJy beam^{-1} and increase in multiples of 2.

4.3 Rotation curve shapes

Given that we have generated the first rotation curves for these cluster galaxies, we now study how the distribution of luminous matter scales with the rotation curve shapes. The distribution of luminous matter is known to affect the shape of the rotation curves for all galaxy types. More luminous galaxies are known to have steep rising rotation curves in the inner parts, followed by a flatter gradient at large radii, and less luminous galaxies (e.g. dwarf galaxies) have been reported to have rotation curves with shallower slopes in the inner regions, rising to the last measured point (e.g. Swaters et al. 2012).

In our work, we look at the M_* of the individual galaxies in an attempt to investigate the variation of the rotation curves at different M_* bins.

In Fig. 9, we present the rotation curves of a subset of nine galaxies with calculated stellar masses (M_*). We study the shapes of these nine rotation curves in three stellar mass bins, as shown in Fig. 9. For galaxies in the stellar mass range of $9.5 < \log_{10}(M_*/{\rm M}_\odot) < 10.5$, the rotation curves exhibit a gradual rise in the inner regions and continue to increase out to the last measured point. This behaviour is consistent with the study of Swaters et al. (2012) and suggests a dominant dark matter component throughout the galaxy. The dark matter halo likely provides the majority of the gravitational potential,

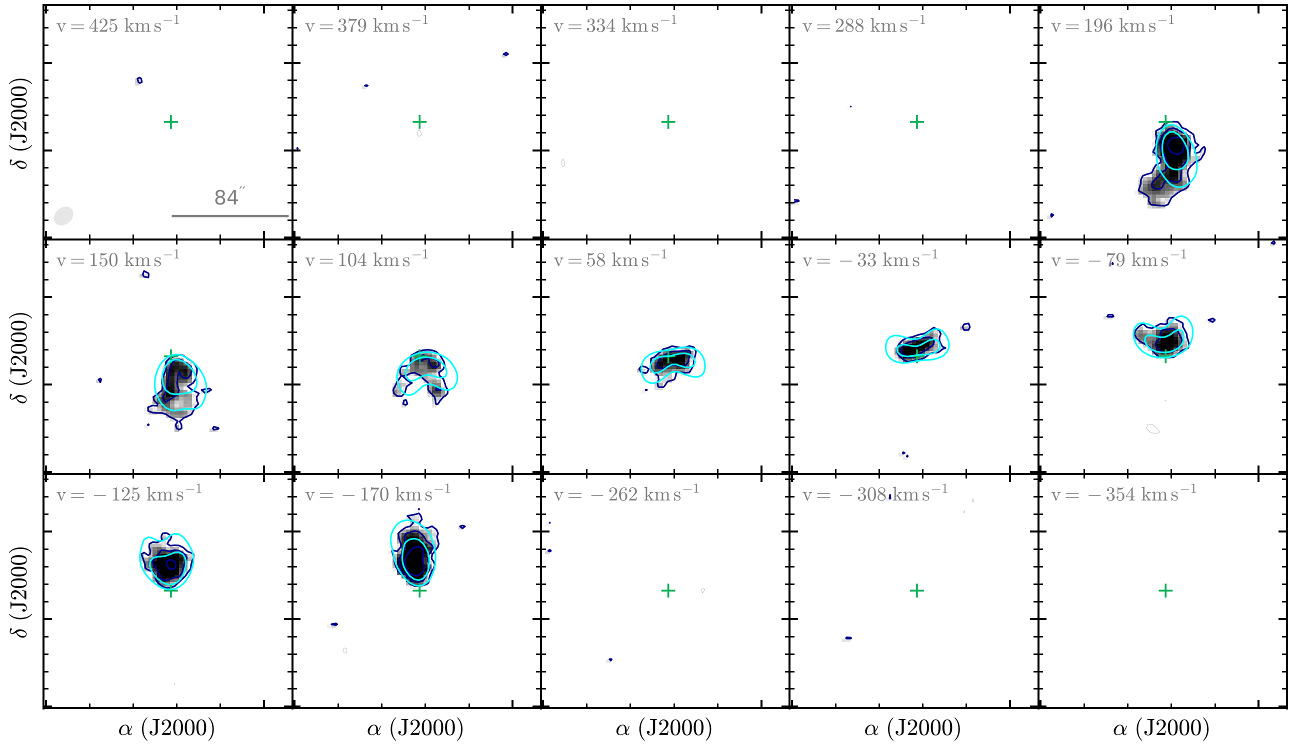

Figure 8. Galaxy ID 26 channel-by-channel comparison of the data, in greyscale with dark-blue contours, and the $^{3\mathrm{D}}$BAROLO model presented with cyan contours. The green cross marks the $^{3\mathrm{D}}$BAROLO model centre coordinates. The MeerKAT synthesized beam (13.1 × 11.7 arcsec^2) is displayed in the top-left panel, with the grey horizontal bar representing the physical scale.

Table 3. Rotation curve data of the 14 galaxies with converged kinematic fits.

ID (1)	r_{out} (kpc) (2)	v_{out} (km s^{-1}) (3)	i (°) (4)	PA (°) (5)	v_{sys} (km s^{-1}) (6)
9	61.54	239.71	44.30	304.62	707.54
13	22.56	201.72	63.64	353.49	559.76
18	23.64	116.72	70.91	109.92	162.87
20	22.92	292.29	71.03	330.24	369.68
21	22.55	174.48	52.93	266.07	491.03
22	22.53	109.02	56.87	228.01	388.59
26	53.15	200.04	67.73	190.22	−384.04
37	22.92	181.22	58.34	86.29	−45.58
38	40.88	145.17	51.71	71.31	−110.76
49	13.75	63.92	36.54	87.51	−653.93
50	31.90	128.91	53.82	41.55	−654.68
51	31.90	186.55	67.16	357.15	−440.94
53	13.67	221.20	44.82	210.10	−764.02
59	41.05	153.96	70.92	261.44	−791.02

resulting in a shallow inner slope and a steadily rising curve at larger radii, where baryonic matter plays a relatively minor role.

For intermediate-mass galaxies, $10.5 < \log_{10}(M_*/\mathrm{M}_\odot) < 11$, the rotation curves also tend to rise throughout the observed radial range. While two galaxies in this mass range appear to show some flattening in the outer regions, this is based on only three rotation curve points per galaxy, with the final two points showing a flat gradient. As such, these cases provide limited evidence for a clear transition to dark matter dominance at large radii. Overall, the general shape of the rotation curves in this mass range does not differ significantly from that of the lower-mass systems in this cluster, possibly indicating that dark matter continues to play a significant role even in the inner regions, or that the stellar and gas contributions are more modest than previously inferred.

For high-mass galaxies, $\log_{10}(M_*/\mathrm{M}_\odot) > 11$, the rotation curves generally flatten at larger radii, consistent with dark matter dominating the outer kinematics. Although a steep central rise could suggest a strong central concentration of baryons, in our sample only one galaxy shows a pronounced inner velocity increase. Furthermore, the coarse velocity resolution (46 km s^{-1}) may lead to residual beam smearing, which can smooth out steep velocity gradients in the innermost regions of the rotation curves.

5 BARYONIC TULLY–FISHER RELATION

We study the bTFr for galaxies with converged kinematic models, examining the V_{out} definition. Following the approach of Ponomareva et al. (2021), we define V_{out} as the rotation velocity at the outermost H I radius. The uncertainties on V_{out} are derived from the uncertainties obtained in the kinematic modelling. The baryonic mass M_{bar} is calculated as

$$M_{\mathrm{bar}} = 1.33 M_{\mathrm{H\,I}} + M_*, \qquad (8)$$

where $M_{\mathrm{H\,I}}$ is the H I mass and M_* is the stellar mass, calculated with equations (1) and (2), respectively. To account for the contribution of helium, we use a factor of 1.33 and neglect the molecular gas as it generally contributes less than 10 per cent of M_{bar} (McGaugh & Schombert 2015). We calculate the uncertainties on M_{bar} following equation (5) of Lelli et al. (2016). We perform a linear fit of the form,

$$\log(M_{\mathrm{bar}}) = \alpha \log(x) + \beta, \qquad (9)$$

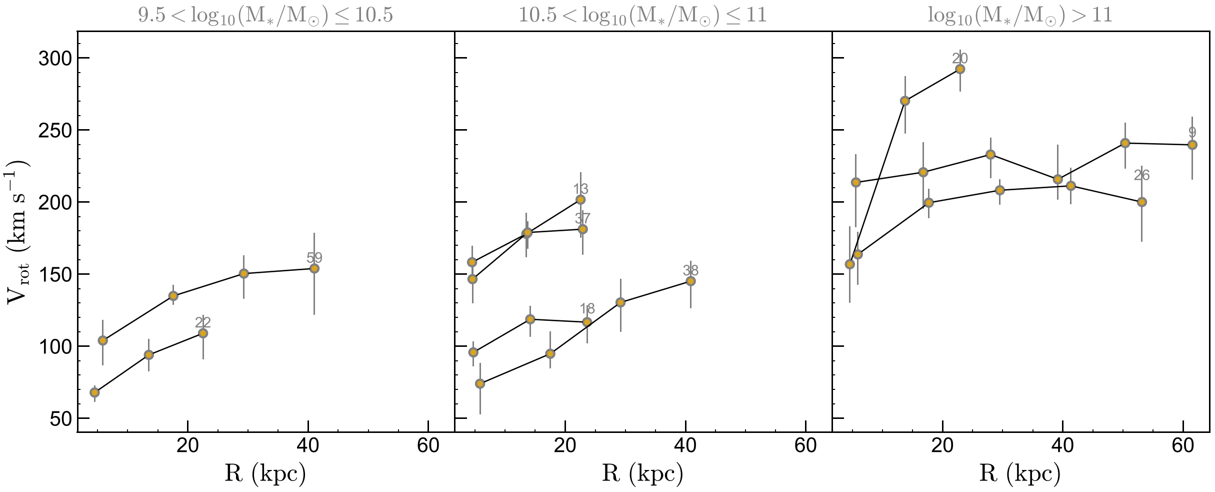

Figure 9. Rotation curves of nine galaxies with calculated stellar masses, at different stellar mass bins.

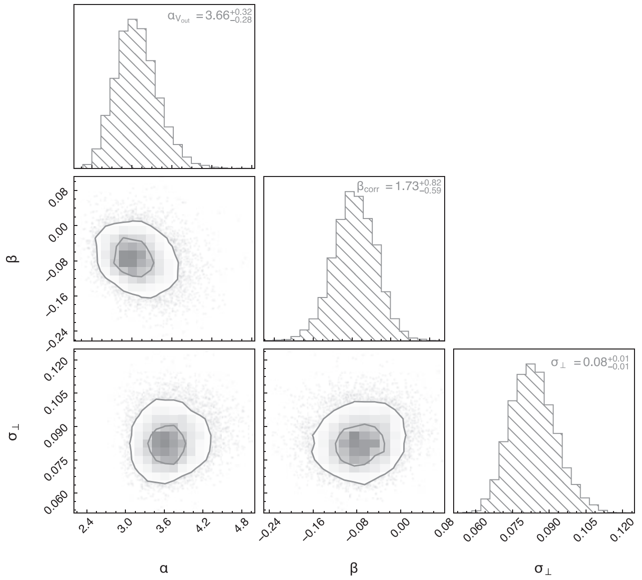

Figure 10. The posterior distributions of the slope (α), zero point (β) and the orthogonal scatter ($\sigma_\perp$) for the bTFR based on V_{out}. The contour levels are at 68 and 95 per cent confidence intervals.

where M_{bar} is the baryonic mass as defined by equation (8), x is the velocity definition, V_{out}, α is the slope, and β is the zero-point.

In this paper, we extend our sample of galaxies with that of Ponomareva et al. (2021), resulting in a total of 79 galaxies, spanning a redshift range $0.006 \lesssim z \lesssim 0.081$. We leverage the methodology described by Lelli et al. (2019). We employ a well-established MCMC technique implemented in EMCEE (Foreman-Mackey et al. 2013) to sample the posterior probability distributions of crucial statistical parameters: α, β, and $\sigma_\perp$. We initialize our MCMC simulation with 50 walkers. Each walker explores the parameter space for three parameters: α, β, and $\sigma_\perp$. To start, the walkers are positioned randomly within predefined ranges that reflect our prior knowledge about these parameters. The values of α can range from 3.0 to 5.0, those of β from 1.0 to 5.0, and those of $\sigma_\perp$ from 0.01 to 0.25, all of which have uniform prior probabilities within these limits. The sampler is then run for 1000 iterations, followed by another 1000 iterations to ensure thorough exploration. Fig. 10 presents the posterior distributions of the fitted parameters for the bTFr. The best-fitting values of the parameters, for both velocity definitions, are presented in Table 4.

Table 4. The fitted statistical properties of the bTFr.

Slope	$3.66^{+0.32}_{-0.28}$
Zero point	$1.73^{+0.82}_{-0.59}$
Intrinsic scatter ($\sigma_\perp$)	$0.08^{+0.01}_{-0.01}$

Fig. 11 shows the bTFr for the combined sample (i.e. 79 galaxies) for the V_{out} velocity definition. We find that the properties of the relation using this velocity definition are consistent with those achieved in Ponomareva et al. (2021). Notably, H I detections from the Abell 3408 galaxy cluster, despite being at relatively low redshifts ($\langle z \rangle \sim 0.042$) extend the bTFr in both mass and velocity space. Several of these Abell 3408 H I detections are falling within the 1σ scatter of the relation, with few seen below and above the relation.

6 SUMMARY AND CONCLUSIONS

In this paper, we use MeerKAT L-band observations to study the kinematics of individual galaxies in the Abell 3408 galaxy cluster at $z \sim 0.042$, $D \sim 187$ Mpc. Using SOFIA (Serra et al. 2015), a total of 64 galaxies are detected in H I in this X-ray luminous cluster. The main results of this work are summarized as follows.

(i) We study the impact of the dense cluster environment on the global properties of the galaxies. We find that galaxies closer to the cluster centre exhibit a higher degree of H I deficiency compared with galaxies seen over a projected distance of $d_{\mathrm{proj}} \sim 0.5$ Mpc. We perform a linear fit to this observed trend and find a relation of $f_g = 0.04 d_{\mathrm{proj}} + 0.88$, with a scatter of 0.012.

(ii) We present rotation curves of cluster galaxies generated in a uniform way. To study the H I kinematics of this sample of galaxies, we develop a semi-automated pipeline that requires little to no manually chosen priors about the galaxy's kinematic parameters and little human intervention. Despite the coarse spatial and velocity resolution (46 km s^{-1}) of the MeerKAT H I datacubes at hand, our pipeline is able to model the rotation and dispersion curves for several galaxies with the produced H I kinematic models consistent with the data.

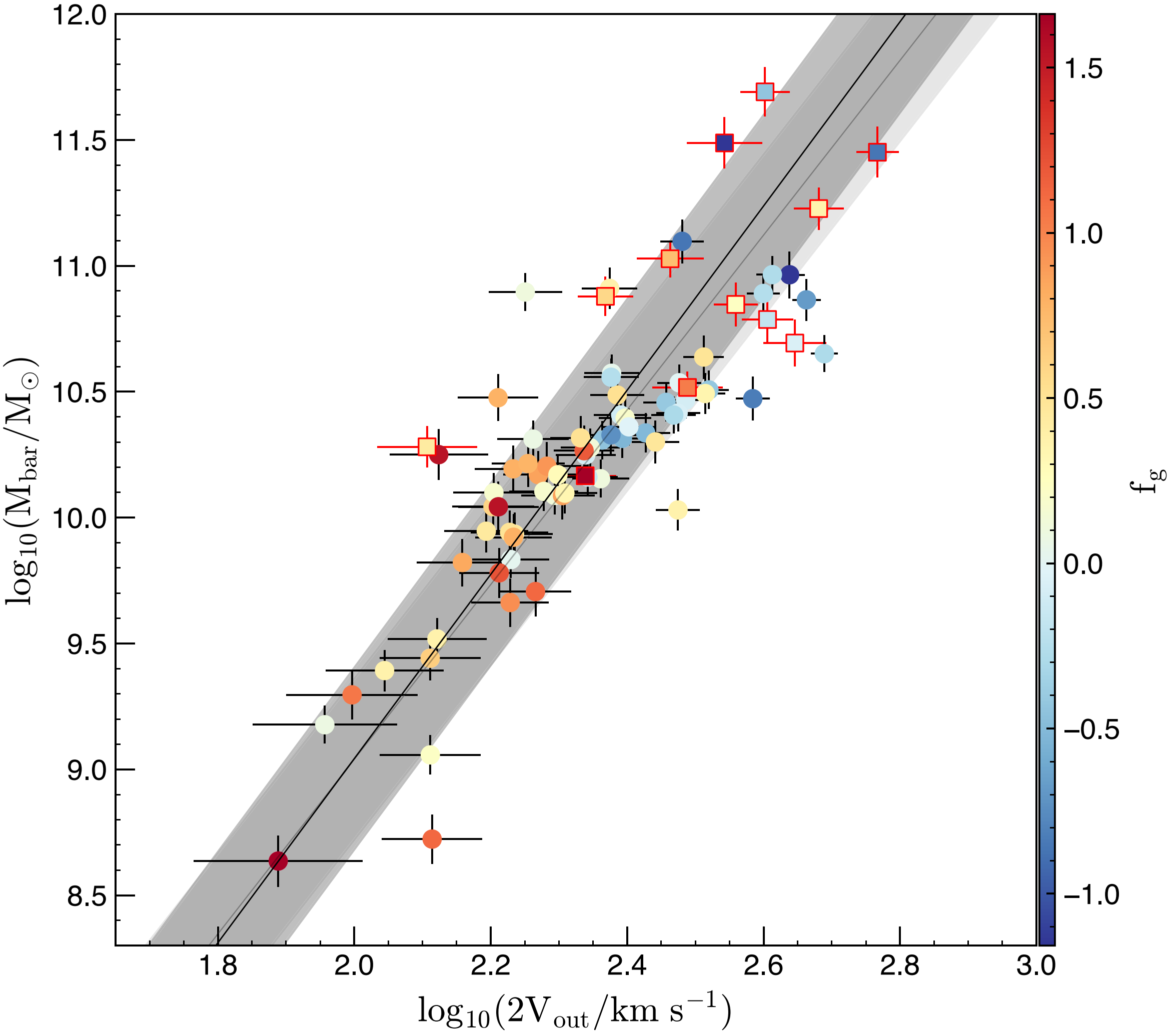

Figure 11. The bTFr for the outermost rotation curve ($V_{\rm out}$) velocity definition. The points are coloured by $f_{\rm g}$, and the black line shows a linear fit to the data. The dark-grey shaded area shows the 1σ uncertainty of the fit. The data points from the MIGHTEE bTFr are shown with circles and squares for the Abell 3408 selected galaxies with converged kinematic fits. The grey line with the light-grey shaded area is the linear fit and 1σ uncertainty of the MIGHTEE bTFr.

(iii) Low-mass galaxies, $\log_{10}(M_*/\mathrm{M}_\odot) < 10$, exhibit rotation curves that rise gradually from the inner regions and continue to increase out to the last measured point, consistent with dark matter dominance throughout their radial extent. Intermediate-mass galaxies, $10 < \log_{10}(M_*/\mathrm{M}_\odot) < 11$, show similar rising rotation curves, with only limited evidence for flattening in the outer regions, seen in two cases with sparse sampling (three data points), making it difficult to draw firm conclusions about baryonic versus dark-matter dominance. High-mass galaxies, $\log_{10}(M_*/\mathrm{M}_\odot) > 11$, display a sharp rise in the central regions, although this feature is seen in only one galaxy and may be affected by beam smearing, limiting strong claims about central baryonic concentration.

(iv) Based on the $V_{\rm out}$ velocity definitions, we study the bTFr in Abell 3408. We extend our sample of galaxies with that of the MIGHTEE Survey Early Science data (Ponomareva et al. 2021), resulting in 79 galaxies in total, spanning a broad range of environments. For the bTFr based on $V_{\rm out}$, we achieve a tight relation $\sigma_\perp = 0.08^{+0.01}_{-0.01}$, which is consistent within errors to the one found in Ponomareva et al. (2021), similarly for the slope and the zero-point. The MeerKAT H I detections from the Abell 3408 galaxy extend the MIGHTEE bTFr in both mass and velocity spaces.

(v) The MeerKAT telescope continuously probes vast cosmological volumes, generating enormous extragalactic data sets. With the upcoming MeerKAT+ and SKA-mid expansions, these data sets will increase dramatically. Therefore, automated tools for detailed analysis of these data sets are essential.

ACKNOWLEDGEMENTS

We thank the anonymous referee for useful and in-depth comments that have greatly improved the quality of this manuscript. The authors would like to thank Anastasia Ponomareva for providing (through private communication) the MIGHTEE bTFr data and for the useful discussions on this section. We would also like to thank Enrico Di Teodoro and Filippo Fraternali for their useful inputs on pyBBarolo and CANNUBI. We would like to thank the staff of the South African Radio Astronomy Observatory (SARAO[3]) who made these observations possible. XN and RPD acknowledge funding from the South African Radio Astronomy Observatory (SARAO), which is a facility of the National Research Foundation (NRF), an

---

[3] www.sarao.ac.za

agency of the Department of Science and Innovation (DSI). RPD's research is funded by the South African Research Chairs Initiative of the DSI/NRF. The MeerKAT telescope is operated by the South African Radio Astronomy Observatory (SARAO), which is a facility of the National Research Foundation, an agency of the Department of Science and Innovation. The authors also acknowledge the use of the Ilifu cloud computing facility (www.ilifu.ac.za), a partnership between the University of Cape Town (UCT), the University of the Western Cape, the University of Stellenbosch, Sol Plaatje University, the Cape Peninsula University of Technology and the South African Radio Astronomy Observatory. The Ilifu facility is supported by contributions from the Inter-University Institute for Data Intensive Astronomy (IDIA; a partnership between the University of Cape Town, the University of Pretoria, the University of the Western Cape and the South African Radio Astronomy Observatory), the Computational Biology division at UCT, and the Data Intensive Research Initiative of South Africa (DIRISA). This work has made use of the Cube Analysis and Rendering Tool for Astronomy (CARTA; Comrie et al. 2021). This research made use of Astropy,[4] a community-developed core Python package for astronomy. This research makes use of the semi-automated MeerKAT data calibration pipeline, OXKAT.[5]

DATA AVAILABILITY

The MeerKAT reduced cubes and derived data products used in this work are available upon request from corresponding authors.

REFERENCES

Abril-Melgarejo V. et al., 2021, A&A, 647, A152

Asad K. M. B. et al., 2021, MNRAS, 502, 2970

Biviano A. et al., 2013, A&A, 558, A1

Boselli A., Cortese L., Boquien M., Boissier S., Catinella B., Gavazzi G., Lagos C., Saintonge A., 2014, A&A, 564, A67

Boselli A., Fossati M., Sun M., 2022, A&AR, 30, 3

Bosma A., 1981, AJ, 86, 1825

Brown T. et al., 2021, ApJS, 257, 21

Caminha G. B., Suyu S. H., Grillo C., Rosati P., 2022, A&A, 657, A83

Catinella B. et al., 2018, MNRAS, 476, 875

Chung A., van Gorkom J. H., O'Neil K., Bothun G. D., 2002, AJ, 123, 2387

Chung A., van Gorkom J. H., Kenney J. D. P., Vollmer B., 2007, ApJ, 659, L115

Cluver M. E. et al., 2014, ApJ, 782, 90

Comrie A. et al., 2021, CARTA: Cube Analysis and Rendering Tool for Astronomy. Astrophysics Source Code Library, record ascl:2103.031

Cortese L., Catinella B., Smith R., 2021, PASA, 38, e035

Courteau S., Andersen D. R., Bershady M. A., MacArthur L. A., Rix H.-W., 2003, ApJ, 594, 208

Davé R., Anglés-Alcázar D., Narayanan D., Li Q., Rafieferantsoa M. H., Appleby S., 2019, MNRAS, 486, 2827

de Blok W. J. G., Bosma A., 2002, A&A, 385, 816

de Blok W. J. G., Walter F., Brinks E., Trachternach C., Oh S. H., Kennicutt R. C., 2008, AJ, 136, 2648

Dénes H., Kilborn V. A., Koribalski B. S., 2014, MNRAS, 444, 667

Di Teodoro E. M., Peek J. E. G., 2021, ApJ, 923, 220

di Teodoro E. M., Fraternali F., 2015, MNRAS, 451, 3021

Foreman-Mackey D., Hogg D. W., Lang D., Goodman J., 2013, PASP, 125, 306

Glowacki M., Elson E., Davé R., 2020, MNRAS, 498, 3687

Gunn J. E., Gott J. R. I., 1972, ApJ, 176, 1

Haynes M. P., Giovanelli R., Chincarini G. L., 1984, ARA&A, 22, 445

Heywood I., Hale C. L., Jarvis M. J., Makhathini S., Peters J. A., Sebokolodi M. L. L., Smirnov O. M., 2020, MNRAS, 496, 3469

Hunter D. A. et al., 2012, AJ, 144, 134

Iorio G., Fraternali F., Nipoti C., Di Teodoro E., Read J. I., Battaglia G., 2017, MNRAS, 466, 4159

Jarrett T. H., Cluver M. E., Taylor E. N., Bellstedt S., Robotham A. S. G., Yao H. F. M., 2023, ApJ, 946, 95

Jarvis M. J. et al., 2017, preprint (arXiv:1709.01901)

Jonas J. L., MeerKAT Team, 2016, in Proceedings of MeerKAT Science: On the Pathway to the SKA. Proceedings of Science

Koopmann R. A., Kenney J. D. P., 2004, ApJ, 613, 866

Koribalski B. S. et al., 2018, MNRAS, 478, 1611

Kravtsov A. V., Borgani S., 2012, ARA&A, 50, 353

Laudage S. et al., 2024, A&A, 690, A169

Lee B. et al., 2016, MNRAS, 466, 1382

Lelli F., Verheijen M., Fraternali F., 2014, A&A, 566, A71

Lelli F., McGaugh S. S., Schombert J. M., 2016, ApJ, 816, L14

Lelli F., McGaugh S. S., Schombert J. M., Desmond H., Katz H., 2019, MNRAS, 484, 3267

Mamon G. A., Cava A., Biviano A., Moretti A., Poggianti B., Bettoni D., 2019, A&A, 631, A131

Mancera Piña P. E., Fraternali F., Oosterloo T., Adams E. A. K., Oman K. A., Leisman L., 2021, MNRAS, 512, 3230

Mancera Piña P. E., Fraternali F., Oosterloo T., Adams E. A. K., Teodoro E. D., Bacchini C., Iorio G., 2022, MNRAS, 514, 3329

Mantz A., Allen S. W., Rapetti D., Ebeling H., 2010, MNRAS, 406, 1759

Marasco A., Poggianti B. M., Fritz J., Werle A., Vulcani B., Moretti A., Gullieuszik M., Kulier A., 2023, MNRAS, 525, 5359

McGaugh S. S., Schombert J. M., 2015, ApJ, 802, 18

McGaugh S. S., Schombert J. M., Bothun G. D., de Blok W. J. G., 2000, ApJ, 533, L99

Moretti A. et al., 2023, ApJ, 955, 153

Munari E., Biviano A., Mamon G. A., 2014, A&A, 566, A68

Nascimento R. S., Ribeiro A. L. B., Trevisan M., Carrasco E. R., Plana H., Dupke R., 2016, MNRAS, 460, 2193

Nipoti C., 2010, in Antonuccio-Delogu V., Silk J., eds, AGN Feedback in Galaxy Formation. Cambridge University Press, Cambridge, p. 194

O'Beirne T. et al., 2024, MNRAS, 528, 4010

Offringa A. R., 2010, AOFlagger: RFI Software. Astrophysics Source Code Library, record ascl:1010.017 (ascl:1010.017)

Ott J. et al., 2012, AJ, 144, 123

Parkash V., Brown M. J. I., Jarrett T. H., Bonne N. J., 2018, ApJ, 864, 40

Piraino-Cerda F. et al., 2023, MNRAS, 528, 919

Planck Collaboration XIII, 2016, A&A, 594, A13

Planck Collaboration VI, 2018, A&A, 641, A6

Poggianti B. M. et al., 2017, Nature, 548, 304

Ponomareva A. A., Verheijen M. A. W., Papastergis E., Bosma A., Peletier R. F., 2017, MNRAS, 474, 4366

Ponomareva A. A. et al., 2021, MNRAS, 508, 1195

Reynolds T. N., Westmeier T., Staveley-Smith L., Chauhan G., Lagos C. D. P., 2020, MNRAS, 493, 5089

Rogstad D. H., Lockhart I. A., Wright M. C. H., 1974, ApJ, 193, 309

Roman-Oliveira F., Fraternali F., Rizzo F., 2023, MNRAS, 521, 1045

Rubin V. C., Ford W. K. J., Thonnard N., 1978, ApJ, 225, L107

Serra P. et al., 2015, MNRAS, 448, 1922

Serra P. et al., 2017, preprint (arXiv:1709.01289)

Swaters R. A., Sancisi R., van der Hulst J. M., van Albada T. S., 2012, MNRAS, 425, 2299

Tasse C. et al., 2018, A&A, 611, A87

Tinker J. L. et al., 2011, ApJ, 745, 16

Tully R. B., Fisher J. R., 1977, A&A, 54, 661

van Albada T. S., Bahcall J. N., Begeman K., Sancisi R., 1985, ApJ, 295, 305

Verheijen M. A. W., 2001, ApJ, 563, 694

Verheijen M. A. W., Sancisi R., 2001, A&A, 370, 765

Vollmer B., Balkowski C., Cayatte V., van Driel W., Huchtmeier W., 2004, A&A, 419, 35

Vulcani B. et al., 2024, A&A, 682, A117

Walter F., Brinks E., de Blok W. J. G., Bigiel F., Kennicutt R. C., Thornley M. D., Leroy A., 2008, AJ, 136, 2563

---

[4] http://www.astropy.org

[5] https://github.com/IanHeywood/oxkat

Wei J. J., 2016, Acta Astronomica Sinica, 57, 504
White M., Cohn J. D., Smit R., 2010, MNRAS, 408, 1818
Wright E. L. et al., 2010, AJ, 140, 1868
Wu H.-Y., Rozo E., Wechsler R. H., 2010, ApJ, 713, 1207
Yu N., Ho L. C., Wang J., 2020, ApJ, 898, 102
Zabel N. et al., 2022, ApJ, 933, 10

APPENDIX A: MEERKAT MOMENT-ZERO MAPS OF ALL THE DETECTIONS

In Fig. A1, we present the MeerKAT H I moment-zero maps for all 64 detections of the Abell 3408 galaxy cluster. The order of the moment zero is by increasing stellar masses.

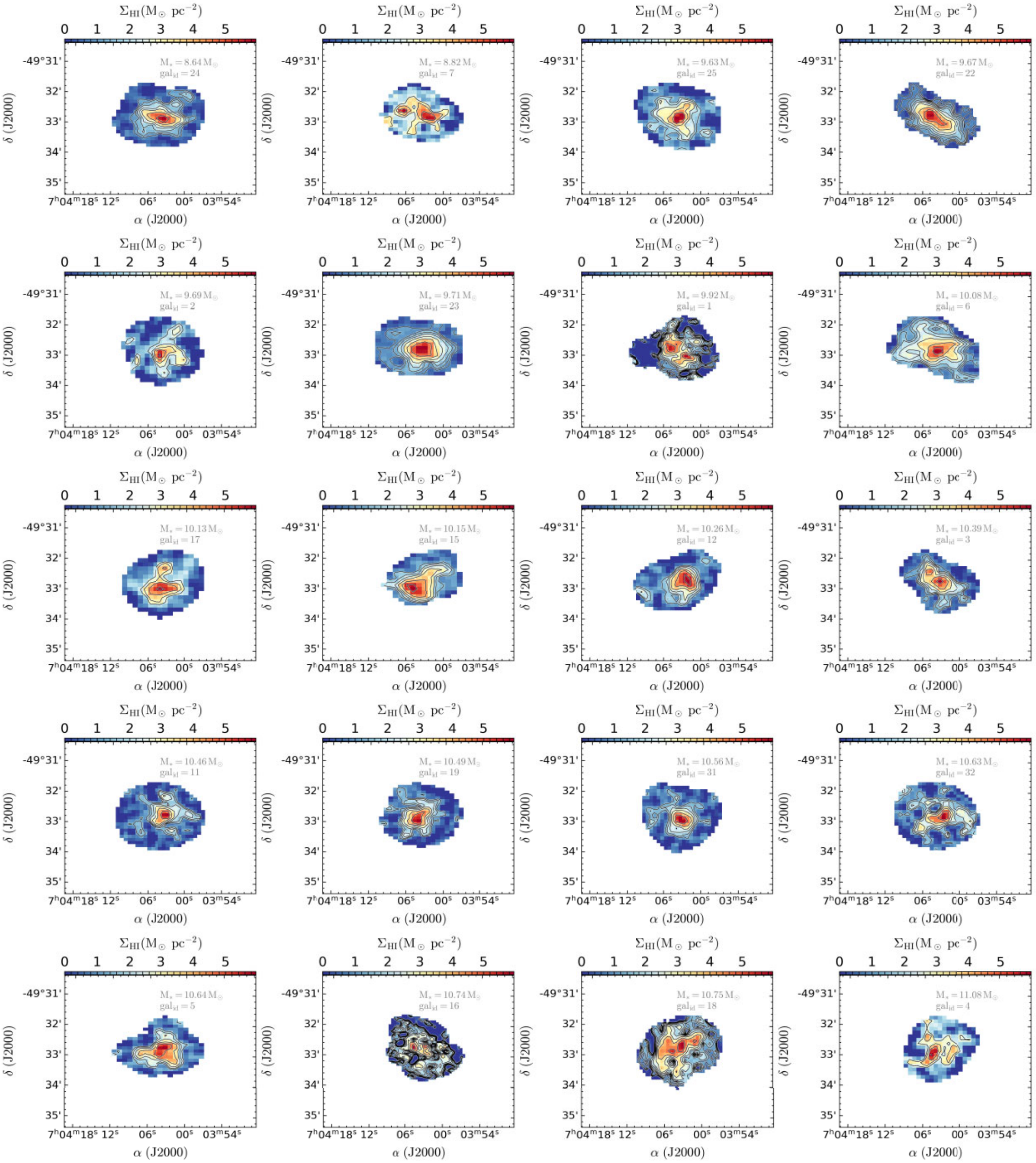

Figure A1. MeerKAT H I moment-zero maps of all 64 detections ordered by increasing stellar masses.

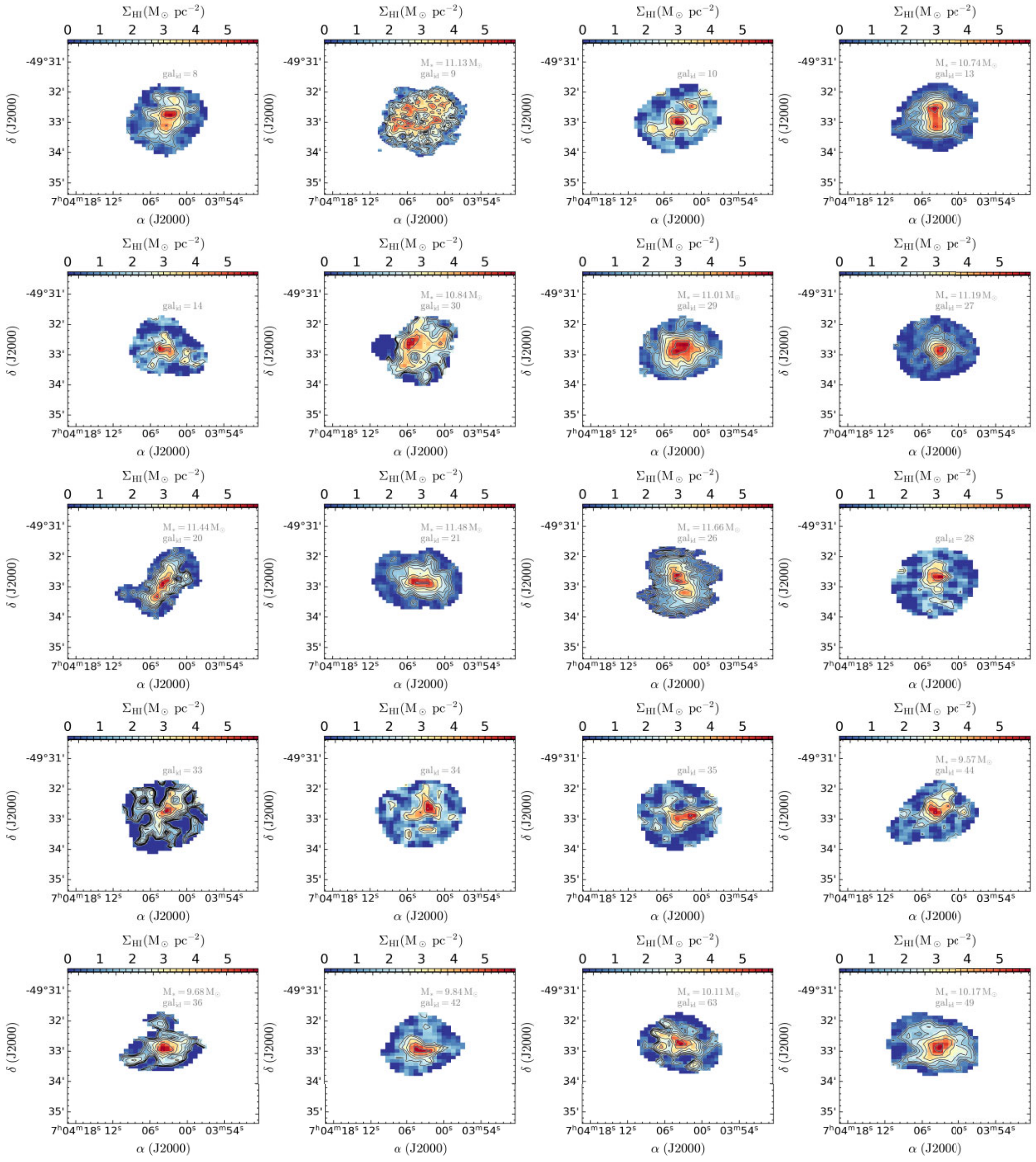

Figure A1. Continued.

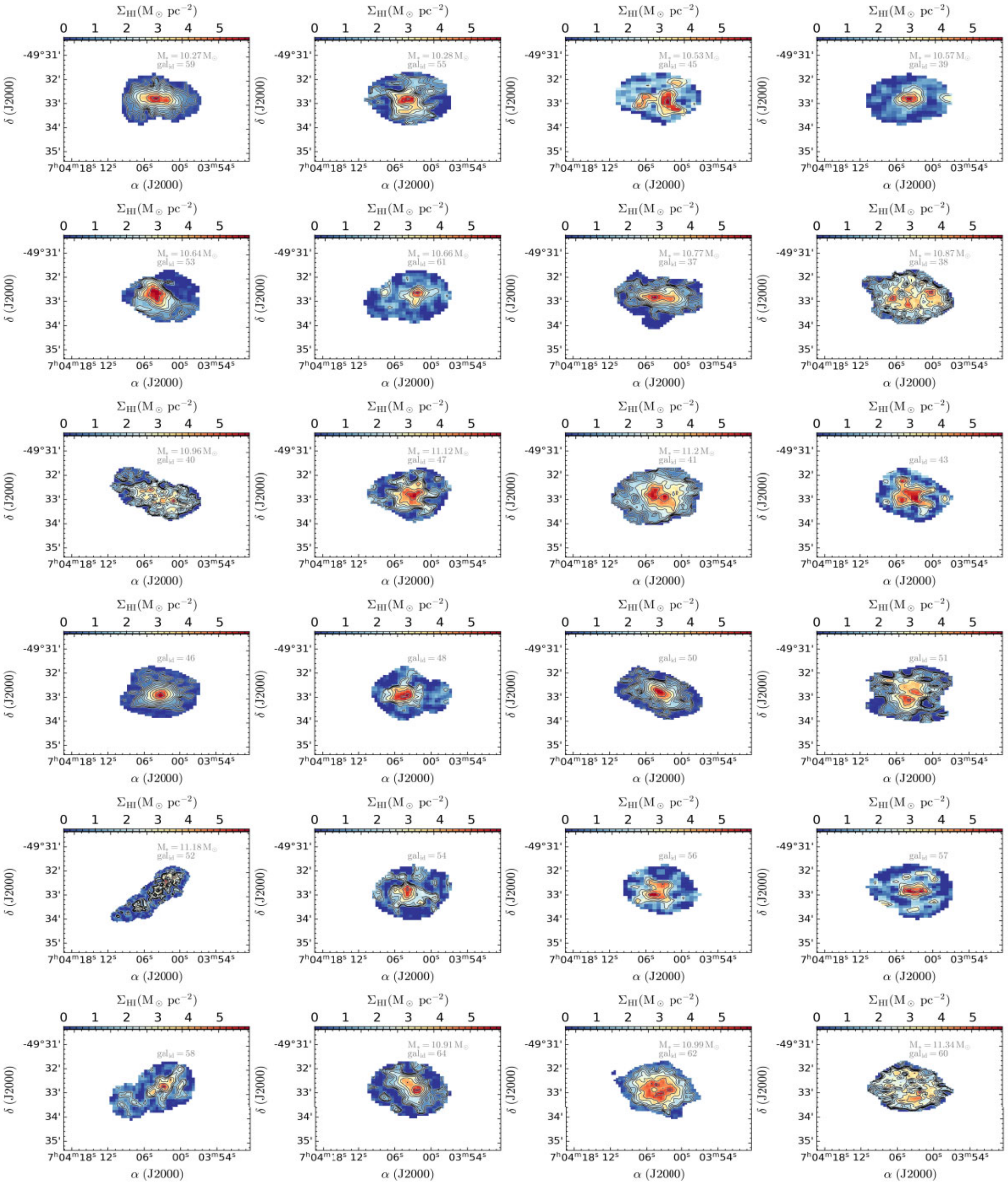

Figure A1. Continued.

This paper has been typeset from a TEX/LATEX file prepared by the author.